ARTICLE

Check for updates

Phase transitions in natural C-O-H-N-S fluid inclusions - implications for gas mixtures and the behavior of solid H$_2$S at low temperatures

Marta Sośnicka [1,2✉] & Volker Lüders[1]

C–O–H–N–S-bearing fluids are known as one of the most challenging geochemical systems due to scarcity of available experimental data. H$_2$S-rich fluid systems were recognized in a wide array of world-class mineral deposits and hydrocarbon reservoirs. Here we report on a nature of low-temperature ($T \geq -192\,°C$) phase transitions observed in natural CH$_4$–H$_2$S–CO$_2$–N$_2$–H$_2$O fluid inclusions, which are modeled as closed thermodynamic systems and thus serve as natural micro-laboratories representative of the C–O–H–N–S system. For the first time, we document solid–solid H$_2$S ($\alpha \leftrightarrow \beta \leftrightarrow \gamma$) transitions, complex clathrates and structural transformations of solid state H$_2$S in natural inclusion gas mixtures. The new data on Raman spectroscopic features and a complete sequence of phase transition temperatures in the gas mixtures contribute to scientific advancements in fluid geochemistry. Enhanced understanding of the phase equilibria in the C–O–H–N–S system is a prerequisite for conscientious estimation of *P-T-V-X* properties, necessary to model the geologic evolution of hydrocarbon and mineral systems. Our findings are a driver for the future research expeditions to extraterrestrial H$_2$S-rich planetary systems owing to their low temperature environments.

[1] GFZ German Research Centre for Geosciences, Telegrafenberg, 14473 Potsdam, Germany. [2] Present address: Institute of Geosciences, Friedrich Schiller University Jena, Burgweg 11, 07749 Jena, Germany. ✉email: marta.sosnicka@uni-jena.de

Hydrogen sulfide (H₂S) is a natural gas of organic or inorganic origin. At shallow crustal levels, it is produced in anaerobic environments by degradation of biomass[1]. As biological mediator H₂S plays an important role in the global sulfur cycle and the evolution of life on Earth[2]. Recent research has shown that H₂S-bearing gaseous fluid inclusions carry information imperative to understanding the building blocks of early Archean life[3]. Inorganic H₂S is a common constituent in volcanic gases[4], active black smoker vents[5], and carbonate-hosted hydrocarbon reservoirs[6–8]. Dissolved in water, H₂S or its dissociation products are indispensable for the formation of precious[9] and base metal deposits[10]. Recent discoveries of H₂S-ice on Uranus and Neptune at temperatures ranging between −220[11] and −153.7 °C[12,13], reveal that the low-temperature conditions, which this study focuses on, find clear analogs in the Solar System. Hence, the processes investigated here are of essential importance for understanding the natural terrestrial as well as extraterrestrial environments. In materials science, H₂S is utilized to synthesize superconductive materials in the form of sulfur hydrides, e.g., H₃S, which displays superconductive properties at transition pressure of 155 GPa and temperature of −70.15 °C[14]. This finding was an important breakthrough in the development of room-temperature CSH₈ superconductor[15].

Determining fluid properties and understanding the phase relations in the P-T-V_m space are paramount in fluid geochemistry and geological sciences[16,17]. Mineral-hosted natural fluid inclusions, which preserve fluids from various geological records in micrometer-scale cavities, are a powerful tool to characterize fluid properties. Fluid inclusions are modeled as "closed" systems, meaning that they permit heat exchange, whereas their molar volumes (V_m) and compositions (X_i) remain constant throughout the geological evolution. Consequently, the P–T conditions of fluid inclusion trapping are deduced from the isochoric trajectories[18], which are constructed from bulk V_m-X_i parameters. Microthermometry allows observation of fluid inclusion phase transition temperatures, which can be converted into V_m and X_i by applying equations of state (EoS) or/and quantitative phase diagrams[19]. Laser Raman spectroscopy allows to determine molecular compositions of complex C–O–H–N–S inclusion gas mixtures[8,10,20–23]. Combined microthermometric and Raman spectroscopic analyses coupled with phase diagrams/EoS provide means to reconstruct the spatial and temporal P–T evolution in mineralizing systems[10,24] and gas reservoirs[8,21,22,25]. The latter are often characterized by multiple episodes of coinciding mineralization and gas/oil re-charge. P–T estimates in such systems rely on the construction of isochores for gaseous and/or aqueous fluid inclusions[26]. This is challenging for CH₄–H₂S–CO₂–N₂ inclusions, which contain elevated H₂S concentrations[27,28] since the properties of the C–O–H–N–S gas mixtures are poorly constrained by experimental and thermodynamic data[29].

Natural H₂S-bearing fluid inclusions representing binary CH₄–H₂S and CO₂–H₂S systems have been characterized in terms of molecular compositions and phase changes[30] as phase equilibria of these two systems are well constrained by experimental studies[31–35]. In contrast, experimental data for ternary system CH₄–CO₂–H₂S are scarce and cover only very limited P–T–X ranges with a focus on the near-critical region of the system[36–38]. An influence of subordinate amounts of CO₂ on phase equilibria in the CH₄–H₂S system in the low-temperature region remains unclear[30,32]. Experimental studies on purified H₂S gas have shown that three structurally distinct solid H₂S phases (I-α, II-β, and III-γ) form at low temperatures below −85.5 °C[39]. Crystal symmetry of the H₂S-γ phase, which forms at the lowest temperatures below −169.6 °C, has been under debate[39–42]. Laser Raman spectroscopy is one of the most effective techniques in

distinguishing structurally distinct solid H₂S molecules[39,42,43]. The structure of H₂S solid phases and solid–solid phase transitions have not been recognized in natural fluid inclusions up to date.

In this study, we investigate fluorite-hosted H₂S-bearing fluid inclusions representing the natural CH₄–H₂S–CO₂–N₂–H₂O system. We use combined microthermometric and Raman spectroscopic analyses to record the complete sequence of phase transition temperatures as well as compositions and spectral features of individual phases at low temperatures.

Results and discussion

Fluid inclusion assemblages. Fluid inclusions were analyzed in line with the classic concept of a fluid inclusion assemblage (FIA)[44]. Both selected FIA's (Fig. 1), consisting of low-density gas-rich (V) and aqueous 2-phase inclusions (L + V), evidence precipitation of fluorite in the presence of methane, inorganic gases (H₂S, CO₂, N₂) as well as small proportions of a high salinity brine. The molecular compositions of gas phases in the gas-rich inclusions are shown in Table 1, Supplementary Table 1, and Source Data.

The two biggest gas-rich inclusions (P1-fi1A, P1a-fi10) in FIA1 contain a visible aqueous film surrounding the gas phase, whereas in the smaller inclusions the aqueous phase is optically invisible. The bimodal distribution, lack of intermediate aqueous fluid/gas ratios, and gas-saturation (in respect of CH₄, CO₂, and H₂S) of the vapor phases of co-existing aqueous brine inclusions imply contemporaneous trapping of immiscible fluids. Fluorite growth from aqueous brine was obstructed by the gas bubbles, which were wet by traces of the aqueous medium during the fluid entrapment. Thus, it is very unlikely to form water-free, pure gas inclusions in such hydrothermal systems. When heating the inclusions to temperatures up to 170 °C, Raman spectroscopic analyses of the homogenized inclusion fluid[45] point to the presence of 3 mol% H₂O in all gas-rich inclusions (Table 1, Supplementary Fig. 1 and Source Data). The volume fractions of the aqueous phase (φ_{H_2O})[46] in two inclusions with optically visible aqueous rim, indicate very similar water contents of 2.2 and 3.5 wt.%. The water vapor or dissolved H₂O was not detected in the gas phase of the gas-rich inclusions at room temperature (Fig. 1a). The gas compositions of six measured inclusions within a single FIA1 (Table 1) are very similar as indicated by very low standard deviation values (σ < 0.02). Median gas compositions for FIA1 are 59 mol% CH₄, 24 mol% H₂S, 10 mol% CO₂, 3 mol% N₂, whereas FIA2 shows a slightly higher H₂S content of 27 mol% (Table 1 and Fig. 1). The aqueous rims of the gas-rich inclusions are H₂S saturated as indicated by the broader Raman peak at 2584 cm⁻¹, which is typical of H₂S dissolved in water at room temperature (Fig. 1b). The origin of low-intensity gas peaks in the latter spectrum is ambiguous, they may be derived from gas species dissolved in water and/or may constitute peak overlaps from a much larger gas phase. The steep band between 3000 and 3700 cm⁻¹, corresponding to the stretching vibrations of H₂O, confirms the high salinity[47] of the aqueous solution coating the gas inclusion (Fig. 1b).

Low-temperature phase transitions—freezing runs. Eight phase transitions were recognized in the studied gas-rich inclusions during freezing (Fig. 2a–i) and heating runs (Fig. 2j–p). The complete temperature sequence of the phase changes is shown in Table 1 and Supplementary Table 2. Two gas-rich inclusions P1-fi1A and P4-fi1B (hereinafter labeled inclusion A and B) of different molecular compositions (Table 1) were used to document in detail the phase transition sequences (Figs. 2 and 3).
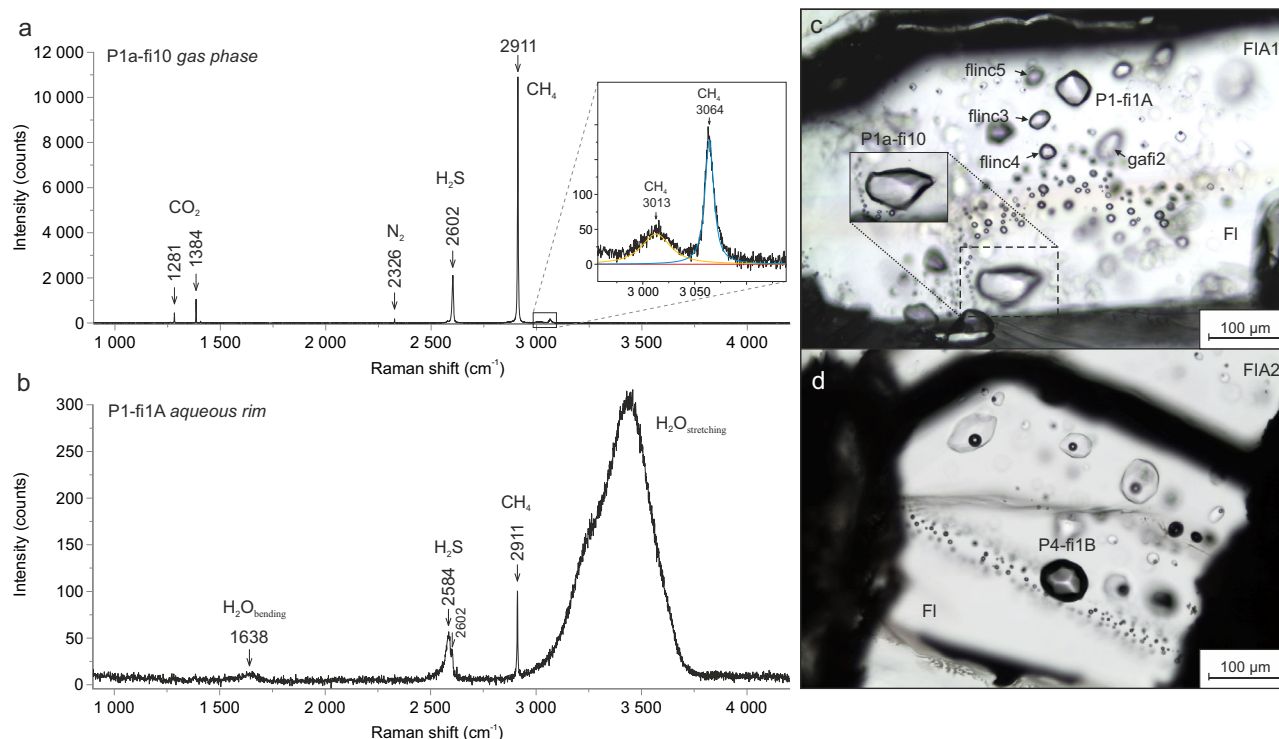
Fig. 1 Fluid inclusion assemblages (FIA's) at room temperature. a Raman spectrum of the gas phase in the gas-rich fluid inclusions shows sharp peaks typical of the gas mixture: CH_4 (2911 cm^{-1}), H_2S (2602 cm^{-1}), CO_2 Fermi diad (1281 cm^{-1}, 1384 cm^{-1}), and N_2 (2326 cm^{-1}), representing symmetric stretching vibrations (ν_1) of the gas molecules. Weak intensity broad peak at 3013 cm^{-1} is attributed to the triply degenerate anti-symmetric C–H stretching of CH_4 gas, whereas a weak $2\nu_2$ overtone at 3064 cm^{-1} is assigned to the doubly degenerate ν_2 mode vibration of CH_4 gas[49]. **b** Raman spectrum of the aqueous phase rim surrounding the gas phase. The broad Raman peak between 3000 and 3700 cm^{-1}, and weak peak at 1638 cm^{-1} correspond to stretching and bending vibrations in H_2O, respectively. The low-intensity Raman band at 2584 cm^{-1} is assigned to H_2S dissolved in water. **c, d** Microphotographs of analyzed CH_4–H_2S–CO_2–N_2–H_2O fluid inclusions in FIA1 and FIA2 hosted in fluorite (Fl).

When cooling the inclusion to temperatures from −17 to −28.7 °C, the first solid phase that nucleates at the corners of the inclusion cavities is H_2S-rich clathrate (Figs. 2b and 3b), which is manifested by two Raman bands at 2593 and 2604 cm^{-1} (Fig. 4). In inclusions, containing a visible water film, the formation of H_2S–CH_4–CO_2–N_2 clathrates is observed (Fig. 4). Raman peaks of 1276 and 1380 cm^{-1} are typical for CO_2-clathrate, bands at 2903 and 2913 cm^{-1} are assigned to CH_4-clathrate, whereas peak splitting to 2324 and 2323 cm^{-1} is attributed to N_2-gas hydrate[48] (Fig. 4a).

During further cooling below −29.9 °C/−32.6 °C (inclusions A/B) the H_2S–CH_4–CO_2–N_2 gas phase begins to shrink due to volume reduction (Figs. 2c and 3c) and partial separation of H_2S-rich liquid. At temperatures of −58.6 °C/−58.5 °C (A/B) CH_4-rich liquid starts to separate from the gas phase (Fig. 2d). The presence of H_2S- and CH_4-rich liquids is indicated by the broadening and shift of the Raman bands to 2593 and 2908 cm^{-1}, respectively. Raman analyses of the three resulting phases reveal that H_2S-rich liquid partitions into the outermost phase, liquid CH_4–CO_2 into the middle phase, whilst CH_4–N_2 gases remain in the innermost bubble (Fig. 3d). At −100 °C, vibrational bands of CH_4–N_2 gases from the innermost phase show a shift to higher wavenumbers (2915 cm^{-1}, 2328 cm^{-1}) compared with the gas phase at room temperature (2911 cm^{-1}, 2326 cm^{-1}) (Fig. 5). Similar peak shifts are observed for CO_2 and H_2S in the middle and the outermost phases, respectively.

At temperatures of −125.1 °C/−117.4 °C (A/B) both H_2S and CO_2 simultaneously freeze and form a fine-grained mass of bright white (CO_2) and yellow-greenish solids (H_2S-α) of high reflectance (Figs. 2e and 3e, f). In order to investigate the composition and phase behavior of the nucleated solids a cycling heating/freezing

method is applied[44]. After melting of solid H_2S, the inclusion is heated further on until only one CO_2 crystal remains. Subsequent rapid cooling results in crystallization of a pure octahedral CO_2 crystal at −100 °C (Figs. 2f and 3g), which shows Raman peaks at 1280 and 1384 cm^{-1}. When cooling the inclusion to about −112 °C numerous oval solids of H_2S-α crystallize. Applying the cycling heating/freezing procedure on H_2S-α is difficult due to the very unstable "jelly-like" behavior of solids and rapid melting of the last solid upon approaching the final T_m(H_2S-α). However, when using slow heating rates (4 °C/min) until only some solids remain in the inclusion and then keeping the temperature constant for several minutes, involuntary re-organization of the leftover solids and formation of a single H_2S-α solid phase is observed (Figs. 3h and 5d). At −110 °C solid H_2S-α shows a single peak at 2558 cm^{-1} (Fig. 6h). Below −184 °C solidification of CH_4 commences (Fig. 2h, i) and is completed at about −185.3 °C/ −186.3 °C (A/B). The resulting CH_4 solid is characterized by a broad band at a vibrational frequency of 2904.5 cm^{-1}. At −190 °C, Raman peaks of CH_4 and N_2 in the remaining squeezed gas phase are shifted towards the highest wavenumbers of 2917 and 2329 cm^{-1}, respectively.

The last optically visible phase change is structural re-configuration of H_2S at about −191 °C. Smooth solids rearrange into very fine-grained polycrystalline aggregates (Fig. 3i, j) over a prolonged period of time, meaning the transition is not instantaneous but requires a few minutes of maintaining the temperature constant. Notable is a prismatic H_2S-γ crystal, tagged with white arrow in Fig. 3i, visible among the fine-grained crystals. This behavior marks the solid H_2S (β → γ) transition, which actually commences at a higher temperature, however, it is not instantly visible under the

Table 1 Microthermometry data and molecular compositions of fluorite-hosted CH_4–H_2S–CO_2–N_2–H_2O fluid inclusions from two fluid inclusion assemblages (FIA's).

Fluid inclusion		Temperature/°C									
		Chip P1 (FIA1)					Chip P4 (FIA2)				
		P1-fi1A	P1a-fi10	gafi2	flinc3	flinc4	flinc5	Median	σ	P4-fi1B
Freezing cycle										
1	Clathrate formation	−28.7	−17	−20	n.o.	n.o.	n.o.	−20	4.96	−21
2	Partial exsolution of H_2S liquid	−29.9	−29.5	−31	−33	−32	−31.9	−31.5	1.22	−32.6
3	Exsolution of liquid CH_4 and gas separation	−58.6	−57.8	−59.6	−59.5	−59.4	−59.1	−59.3	0.63	−58.5
4	Simultaneous freezing T_n of H_2S and CO_2	−125.1	−124.2	−120.5	−114.9	−125.9	−114.9	−122.4	4.58	−117.4
5	H_2S freezing in the presence of solid CO_2	−104	−105.6							−107
6	Solid H_2S-α → solid H_2S-β transition		−149.6[a]							−154.5[a]
7	Solid H_2S-β → solid H_2S-γ transition		−176.8[a]							−175.6[b]
8	CH_4 freezing T_n	−185.3	−188	−187	−186.8	−185.5	−185.7	−186.3	0.97	−186.3
Heating cycle										
9	Final melting T_m (CH_4)	−184.5	−185	−184.2	−184.1	−184.3	−184.2	−184.3	0.30	−185
10	Solid H_2S-γ → solid H_2S-β transition		−168.9[a]							−168.1[b]
11	Solid H_2S-β → solid H_2S-α transition		−147[a]							−146.4[a]
12	Final melting T_m (H_2S)	−98.8	−98.8	−98.9	−98.9	−98.8	−98.9	−98.9	0.05	−99.2
13	Final melting T_m (CO_2)	−91.2	−91.2	−94.5	−91.5	−92.4	−92.2	−91.9	1.14	−92.6
14	Partial homogenization T_{h1} ($L_1L_2V → LV$)	−58.4	−57.6	−59.5	−59.8	−58.7	−58	−58.6	0.78	−57.8
15	Total homogenization T_{h2} ($L_2V → V$)	−28.6	−29.1	−29.2	−32.5	−29.2	−29	−29.2	1.31	−31
16	Final melting T_m (clathrate)	21.8	27.1	23.7	-	-	-	23.7	2.19	27.5
Bulk compositions (mole fractions)										
	$X(CH_4)$	0.59	0.59	0.59	0.60	0.60	0.54	0.59	0.02	0.58
	$X(N_2)$	0.03	0.03	0.03	0.03	0.03	0.04	0.03	0.004	0.03
	$X(CO_2)$	0.11	0.11	0.11	0.10	0.10	0.14	0.10	0.015	0.09
	$X(H_2S)$	0.24	0.24	0.24	0.24	0.24	0.25	0.24	0.005	0.27
	$X(H_2O)$	0.03	0.03	0.03	0.03	0.03	0.03	0.03	0.002	0.03

Temperatures of phase transitions were measured during freezing and heating cycles during coupled microthermometric and Raman spectroscopic analyses without applying the cycling technique (with exception of phase change no. 5 and H_2S solid-solid transitions). See also Source Data file.
n.o. -not observed, L_1-CH_4, L_2-H_2S.
[a]Average from ≥2 measurements.
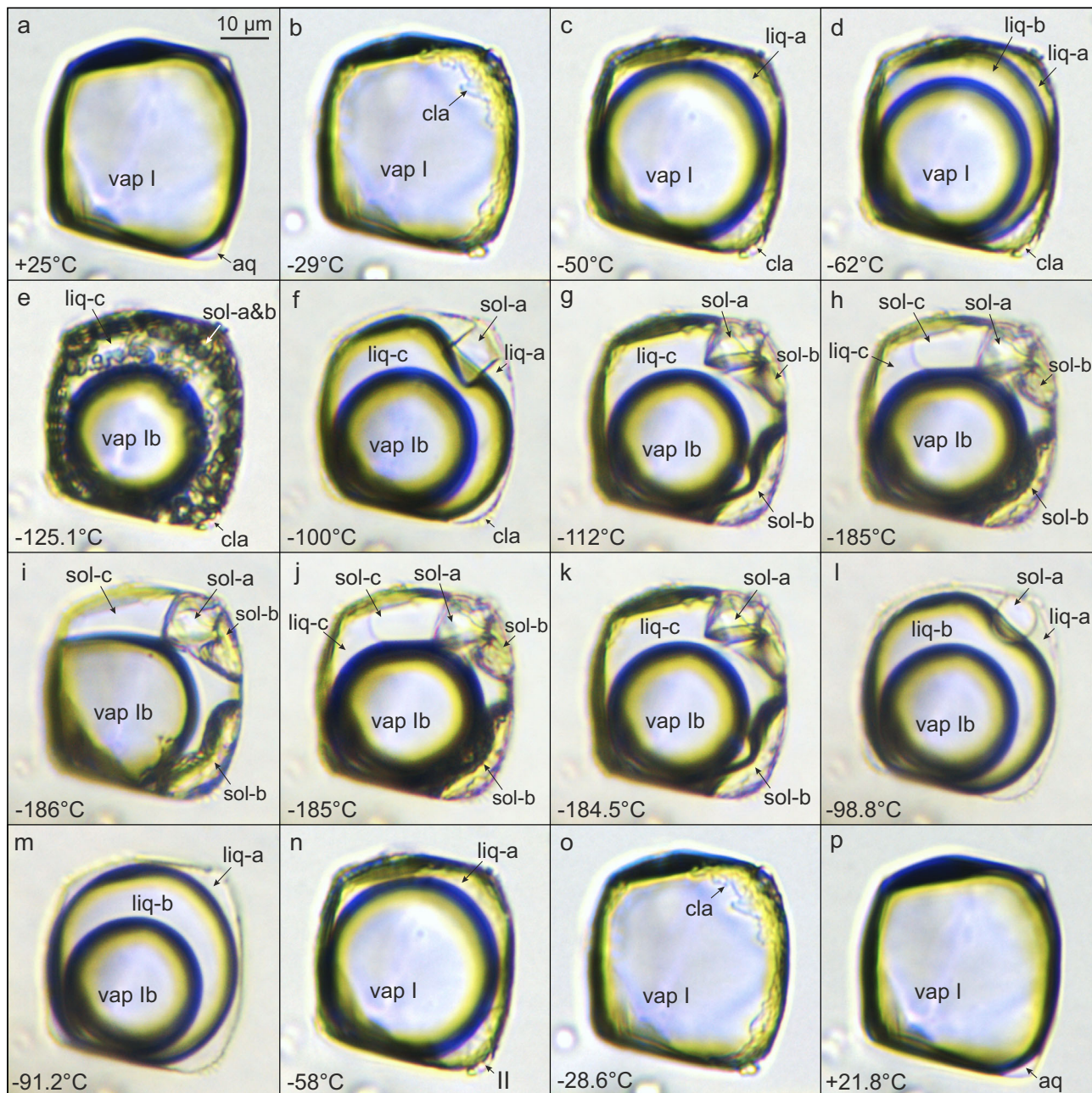[b]Average from ≥15 measurements, also see Supplementary Table 1.

Fig. 2 Transmitted light microphotographs of phase transitions in CH_4–H_2S–CO_2–N_2–H_2O fluid inclusion (no. P1-fi1A) during freezing and heating runs. a One-phase gas inclusion (vap I) at room temperature. **b** Clathrate (cla) formation as a result of the aqueous rim (aq) wetting the gas inclusion. **c** Exsolution of liquid H_2S phase (liq-a). **d** Unmixing of liquid CH_4-CO_2 phase (liq-b). **e** Instantaneous and simultaneous crystallization of liquid H_2S and liquid CO_2 into a fine-grained ice mass. **f** Nucleation of an octahedral CO_2 crystal (sol-a) in the presence of liquid H_2S (liq-a) produced by heating-freezing cycling run. **g** Nucleation of two "blobby" H_2S solids (sol-b) in the presence of liquid CH_4 (liq-c), by applying cycling technique. **h** Continuous solidification of methane with visible solid/liquid methane (sol-c/liq-c) phase boundary. **i** Co-existence of three solid phases: CH_4 (sol-c), H_2S (sol-b), CO_2 (sol-a) and CH_4-N_2 gas phase (vap Ib). **j**, **k** Continuous liquefaction of solid CH_4 (sol-c) until completion at −184.5 °C. **l** Rounded CO_2 solid (sol-a) in the presence of liquid H_2S (liq-a) after H_2S solid melted at −98.8 °C. **m**, **n** Post-CO_2 solid melting at −91.2 °C, continuous vaporization of liquid CH_4-CO_2 phase (liq-b), which is finalized by partial homogenization to a vapor phase (vap I). **o** Vaporization of liquid H_2S (liq-a) finalized by total homogenization to a vapor phase (vap I) at −28.6 °C. **p** Melting of clathrate (cla) at +21.8 °C. Symbols and abbreviations: vap-gas phases: vap I: CH_4–H_2S–CO_2–N_2, vap Ib: CH_4–N_2; cla-clathrate; liq-liquid phases: liq-a: H_2S, liq-b: CH_4-CO_2, liq-c: CH_4; sol-solid phases: sol-a: CO_2, sol-b: H_2S, sol-c: CH_4; aq-aqueous solution.

optical microscope. The median temperature range for the H_2S (β → γ) transition is between −175.1 and −176.1 °C, which gives an overall median of −175.6 °C and $\sigma = 1.27$ (Supplementary Table 2). The transformation to H_2S-γ in the studied inclusion is reflected by the appearance of six characteristic peaks at the following wavenumbers: 2523, 2541, 2545, 2547, 2552, and 2556 cm^{-1} (Figs. 6 and 7). The lower intensity five peaks on the high-frequency side of the Raman spectrum (Fig. 7) develop in an expense of the major H_2S-β peak by decrease in its intensity (Fig. 6). These results are reproducible as H_2S (γ ↔ β) transitions have been observed multiple times during real-time Raman spectroscopic analyses (Supplementary Table 2).

Low-temperature phase transitions—heating runs. When heating the inclusion from −192 °C, eutectic melting of solid CH_4 is observed at about −185.5 °C until the final T_m of −184.5 °C/ −185 °C (A/B) is reached (Fig. 2j-k). At about −168.1 °C (B), a rapid decrease in a band number of the H_2S solid in the Raman spectrum is observed (Fig. 6). This sharp spectrum change reflects the transition of ordered H_2S-γ into the disordered H_2S-β phase.

This conversion is detectable using the Raman technique only as the textural change is not instantly optically visible. The latter proceeds gradually over time (Fig. 6) and commences at temperature as low as −177 °C (Supplementary Table 2). The median temperature range for the H_2S (γ → β) transition lies between −168.9 and −167.5 °C, whereas the median from all measurements is −168.1 °C (σ = 1.62, Supplementary Table 2). Upon
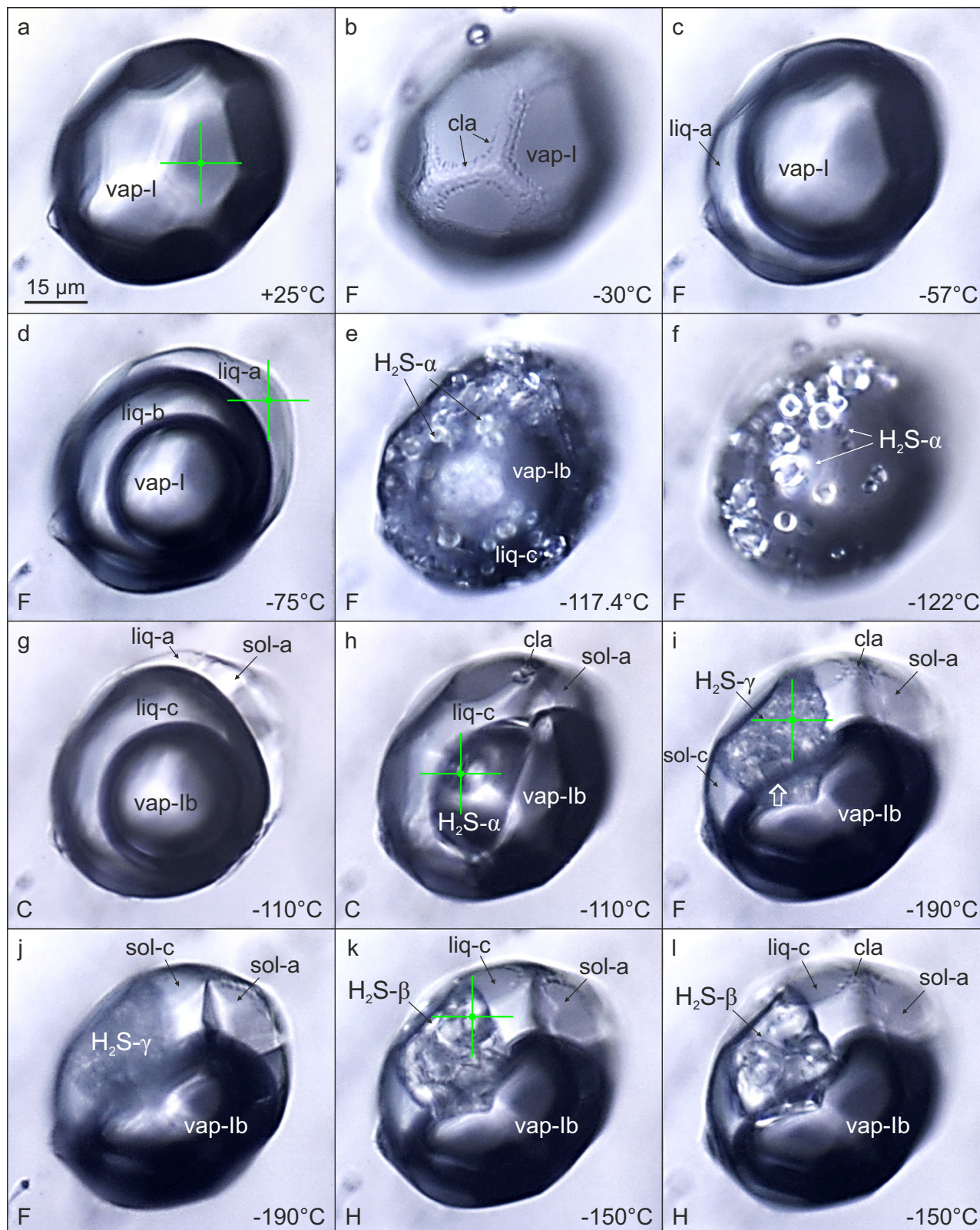
Fig. 3 Microphotographs of phase transitions in CH₄–H₂S–CO₂–N₂–H₂O fluid inclusion (no. P4-fi1B) in the temperature range between +25 and −190 °C, PPL, reflected light. a One-phase gas inclusion (vap-I) at room temperature. **b** Formation of clathrate (cla) at the fluid inclusion corners coated by an aqueous solution. **c** Exsolution of liquid H₂S phase (liq-a). **d** Advanced stage of unmixing of liquid CH₄–CO₂ phase (liq-b). **e, f** Instantaneous and simultaneous crystallization of liquid H₂S and liquid CO₂. **g** Nucleation of solid octahedral CO₂ crystal (sol-a) in the presence of liquid H₂S (liq-a) by applying the cycling technique. **h** Nucleation of a large, oval H₂S solid (H₂S-α) via applying the cycling technique. **i, j** Co-existence of polycrystalline solid H₂S (H₂S-γ), solid CO₂ octahedral crystal (sol-a), solid CH₄ (sol-c), clathrate (cla) and CH₄-N₂ gas phase (vap-Ib), a prismatic H₂S-γ crystal is tagged with a white arrow. **k, l** Appearance of solid H₂S after γ → β phase transformation, visible is structure change from ordered polycrystalline to disordered "blobby" during the heating run. Symbols and abbreviations: vap-gas phases: I: CH₄-H₂S-CO₂-N₂, Ib: CH₄-N₂; cla-clathrate; liq-liquid phases: liq-a: H₂S, liq-b: CH₄–CO₂, liq-c: CH₄; sol-solid phases: sol-a: CO₂, H₂S-α,β,γ: H₂S, sol-c: CH₄; F-freezing run, C-cycling run, H-heating run. Green crosses mark several of Raman measurement points (see also Fig. 6).
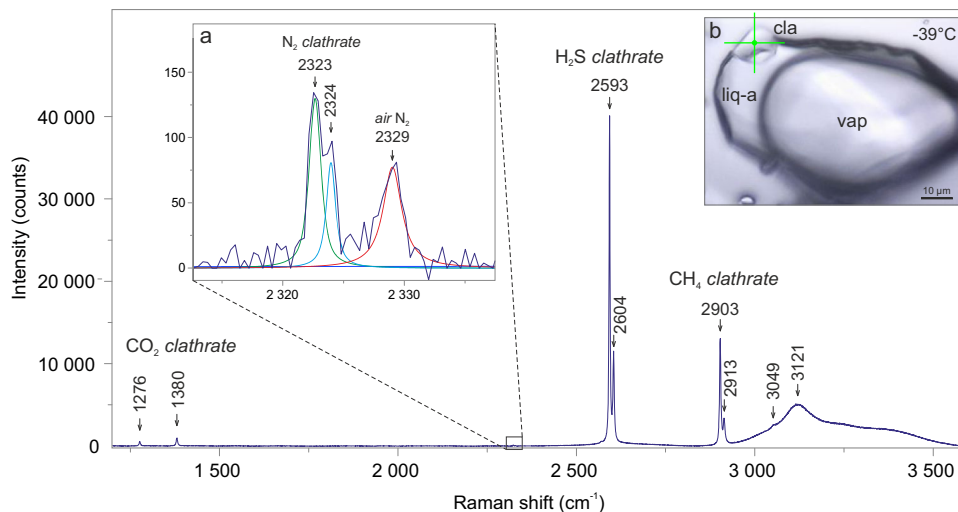

Fig. 4 Raman spectrum of natural clathrate in CH₄-H₂S-CO₂-N₂-H₂O fluid inclusion (no. P1a-fi10) at −39 °C. An individual measurement records complex clathrate phase/s containing H₂S, CH₄ and minor CO₂, N₂ molecules. Additional Raman peaks at 3049 and 3121 cm⁻¹, present in the O-H stretching spectral region, are assigned to a molecular vibration of CH₄ occluded in the hydrate lattice[49] and ice, respectively. **a** The inset shows low-intensity Raman bands corresponding to N-N stretching vibrations in N₂-gas hydrate[48] and air N₂. **b** Microphotograph of the analyzed clathrate solid in gas-rich inclusion. Symbols: vap-CH₄–H₂S–CO₂–N₂ gas phase, cla-measured clathrate phase, liq-a-liquid H₂S phase, the measurement point is marked with a green cross. The spectrum was acquired with 100% laser power.

further heating solid H₂S (β → α) transition at about −146.4 °C (B) is marked by a very slight Raman peak shift from 2549 to 2554 cm⁻¹ and disappearance of the tail at the higher wavenumber side. During heating runs the structure of solid H₂S phases re-organizes itself by compartmentalization of fine-grained crystals into coarser aggregates (e.g., Fig 3k, l) in order to attain back the disordered form. Solid H₂S-α dissolves at −98.8 °C/−99.2 °C (A/B), whereas CO₂ solid remaining in the inclusion does not preserve its octahedral habit but a rounded shape (Fig. 2l) and melts at temperatures of −91.2 °C/−92.6 °C (A/B). After CO₂ melting the inner CH₄–N₂ gas phase begins to expand continuously (Fig. 2m) and partially homogenizes into a vapor phase at $T_{h1}(L_1L_2V \rightarrow L_2V) = -58.4 °C/-57.8 °C$ (A/B, Fig. 2n). The bubble expansion lasts until total homogenization at $T_{h2}(L_2V \rightarrow V) = -28.6 °C/-31 °C$ (A/B, Fig. 2o) is reached. The last observed change is the melting of H₂S-rich gas hydrate (clathrate) at positive temperatures of 21.8 °C/27.5 °C (A/B, Fig. 2p).

Gas hydrates. Gas hydrate crystallizes from the aqueous film containing dissolved H₂S (Fig. 1b) and it forms a shell surrounding the gas phase (Fig. 2b). As a result, the H₂S molecules become encased by the hydrogen-bonded cages in the first place and clathrate cavities are dominated by H₂S. This is evidenced by the highest intensity of the 2592 and 2604 cm⁻¹ Raman peaks, which are assigned to the symmetric H–S stretching vibrations (ν₁) within large cages (LC) and small cages (SC), respectively, of

type I cubic lattice structure (sI)[49]. The characteristic clathrate solid (Fig. 4) is achieved by using a heating/freezing cycling technique, which is applied routinely in the experimental studies of gas hydrates[50]. The H₂S-dominated clathrate (Fig. 4) dissociates at temperatures between +21.8 and +27.5 °C (Table 1), which are lower compared to the quadruple point of the H₂O–H₂S system ($Q_2 = +29.55$ °C[51]). The Raman technique has also been used to identify the H₂S-clathrate in synthetic H₂O–H₂S inclusions at −100 °C[52], in natural CO₂–H₂S–H₂O–S inclusions[53] and at −140 °C in natural H₂S-bearing brine inclusions[54].

A single measurement of one individual, well-isolated clathrate crystal reveals the presence of CH₄ and minor concentrations of CO₂ and N₂ besides H₂S molecules (Fig. 4). This observation suggests crystallization of H₂S–CH₄–CO₂–N₂ mixed gas hydrate. The average cage occupancy ratios – θ_{SC}/θ_{LC} of CH₄- and H₂S-hydrates[49], calculated from deconvoluted Raman spectra, are: 0.81 ($\sigma = 0.08$) and 0.87 ($\sigma = 0.05$), respectively. These values deviate from ratios typical of pure CH₄ and H₂S gas hydrates[49,55], probably due to incorporation of minor CO₂ and/or N₂, which affects relative cage occupancy in the clathrate lattice. The studied clathrate crystal is most likely composed of two clusters of mixed gas hydrates, i.e., the H₂S-dominated clathrate, which grew within the aqueous rim, and CH₄-dominated, which developed at the water–gas interface. The N₂ molecules may occupy both small and large cavities in sI gas hydrates, as indicated by the Raman band splitting (Fig. 4a), whereas CO₂ can occupy only large cages due to the absence of a similar peak splitting (Fig. 4).
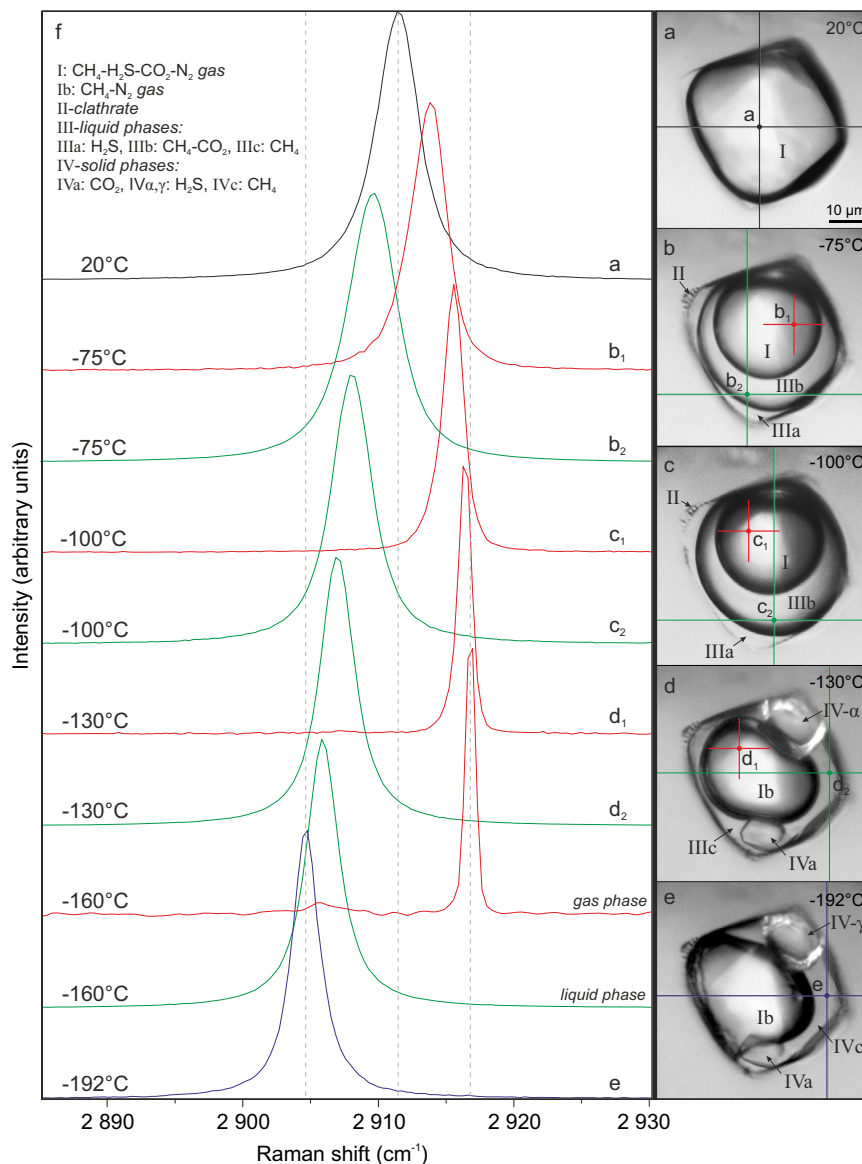
Fig. 5 Raman spectra of symmetric stretching (ν_1) region of CH_4 gas in a natural CH_4–H_2S–CO_2–N_2–H_2O fluid inclusion gas mixture (no. P1-fi1A) at low temperatures. a–e Microphotographs of measured individual phases in analyzed gas-rich inclusion. **f** Sequence of Raman spectra showing that with decreasing temperature Raman peak positions of the exsolved liquid and gas methane shift to lower and higher wavenumbers, respectively. This is a result of relative density increase/decrease during differential partitioning between co-existing phases. The FWHM of the Raman peaks also decrease with decreasing temperatures. Symbols: I: CH_4–H_2S–CO_2–N_2 gas, Ib: CH_4–N_2 gas, II-clathrate, III-liquid phases: IIIa: H_2S, IIIb: CH_4–CO_2, IIIc: CH_4, IV-solid phases: IVa: CO_2, IVα,γ: H_2S, IVc: CH_4, measurement points of different phases are marked with large and small crosses.

Nevertheless, the distribution of CO_2 and N_2 molecules between the clathrates remains ambiguous.

Clathrate crystallization from the aqueous phase, containing the dissolved gas, as well as at the water–gas interface leads to depletion of available water molecules. The nucleation of gas hydrates is known to influence phase equilibria in fluid inclusions, e.g., it may decrease T_m of gas components[17]. Due to the absence of dissolved/vapor H_2O in the gas phase, the only process that may affect the gas phase density is the scavenging of gas molecules into the clathrate lattice at the water–gas interface. The water film likely has a negligible impact on the gas phase transitions as they are very consistent within FIA1 (Table 1), e.g., T_m's of H_2S ($\sigma = 0.05$) or CH_4 ($\sigma = 0.3$). The interaction at the aqueous film-gas phase interface has also some more limitations, e.g., the presence of dissolved H_2S and high salinity of an aqueous solution (Fig. 1b), which decreases the chemical potential of H_2O

resulting in a "salting out" effect[17,56]. Based on the above, it is apparent that only very low amounts of CO_2 and CH_4 from the gas phase have been incorporated into the clathrate lattice at low temperatures, and thus the gas phase experienced only a very minor volume change. Thereby the studied CH_4–H_2S–CO_2–N_2–H_2O system behaves as a gas sub-system below nucleation temperature of clathrate and is interpreted as such in the following section. Applying the isochoric behavior of H_2O-free systems to aqueous-multivolatile inclusions at low temperatures is justified as the LCEP (lower critical end-point) coincides with the critical point of the gas mixture[17]. Median compositions of the gas phase in the presence of stable clathrate at −10 °C are: 58.9 mol% CH_4, 25.5 mol% H_2S, 12.6 mol% CO_2, 2.9 mol% N_2, (FIA1), and 57.1 mol% CH_4, 28.2 mol% H_2S, 11.9 mol% CO_2, 2.9 mol% N_2 (FIA2) (Supplementary Table 1 and Source Data).
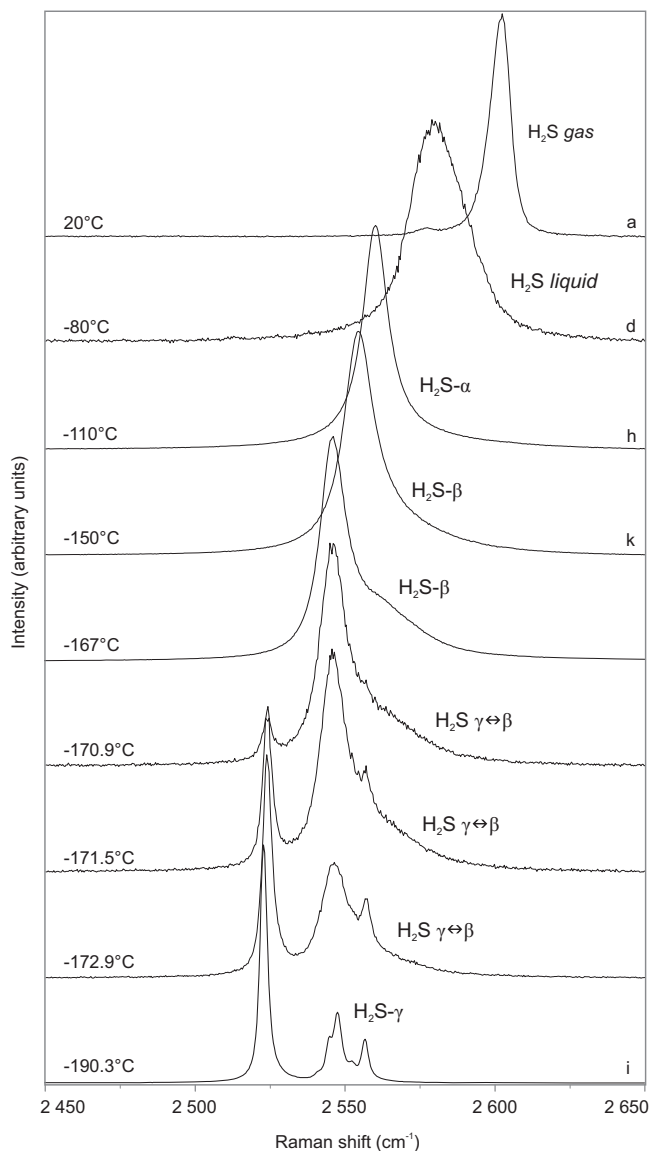
Fig. 6 Raman spectra of the stretching region of H$_2$S in a natural CH$_4$–H$_2$S–CO$_2$–N$_2$–H$_2$O fluid inclusion (no. P4-fi1B) at low temperatures. A density-related shift in Raman peak positions to lower wavenumbers with decreasing temperature is observed for different physical states of H$_2$S. The measurement points (a, d, h, k, i) are indicated by green crosses in the Fig. 3. The solid H$_2$S (γ ↔ β) phase transition is marked by intensity decrease of the characteristic peak of the β-phase and the progressive emergence of the sharp γ-phase peak at the lower wavenumber (2523 cm^{-1}) and its subsequent intensity increase. The solid H$_2$S (γ ↔ β) phase transition was recorded during real-time measurements.

The CH$_4$–H$_2$S–CO$_2$–N$_2$ gas system. A phase diagram defining phase transitions in the multicomponent CH$_4$–H$_2$S–CO$_2$–N$_2$ system has neither been experimentally nor numerically developed so far. The behavior of CH$_4$–H$_2$S–CO$_2$ mixtures, previously observed in fluid inclusions[30,57], was interpreted in the frame of the CH$_4$–H$_2$S system[31] under the assumption that 10–20 mol% CO$_2$ should not significantly affect the phase boundaries. In our study the available P–T projections of phase boundaries of the CH$_4$–H$_2$S–CO$_2$, CH$_4$–H$_2$S, and H$_2$S systems are used to discuss the phase transitions in natural fluid inclusions. The CH$_4$–H$_2$S binary diagram[31] is utilized to interpret the phase behavior to −100 °C, whereas for lower temperatures, the numerically derived CH$_4$–H$_2$S phase diagram[35] and the phase boundaries for pure
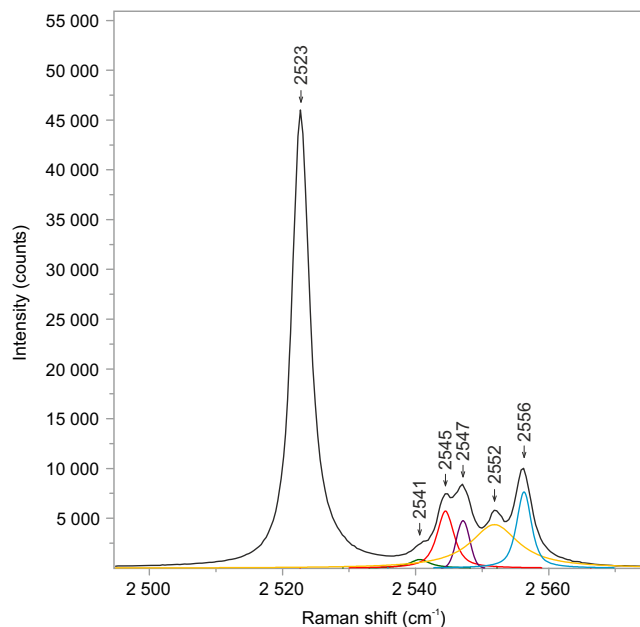

Fig. 7 Raman spectrum of solid H$_2$S-γ in a natural CH$_4$–H$_2$S–CO$_2$–N$_2$–H$_2$O fluid inclusion (no. P4-fi1B). Six characteristic peaks are observed in the H–S spectral region at −191 °C. Five overlapping peaks have been deconvolved into separate bands and fitted using the Gaussian–Lorentzian peak-fitting function. The spectrum was acquired with 100% laser power.

H$_2$S system in the low-pressure region[40] are used (Fig. 8). Fluid inclusion behavior above −60 °C cannot be explained by the CH$_4$–H$_2$S system alone, therefore for this temperature region we use partial ternary CH$_4$–H$_2$S–CO$_2$ phase diagram[58]. Experimentally derived phase boundaries for a CH$_4$–H$_2$S–CO$_2$ system were defined only for a gas mixture with H$_2$S content of 40.2 mol%[58], which is higher than that in studied inclusions (25–28 mol%, Table 1 and Source Data), and CO$_2$ content of 9.87 mol%, which is close to CO$_2$ concentrations in the inclusions (11.9–13.3 mol%, Supplementary Table 1). This P–T phase diagram, based on the experimentally studied gas mixture, is, therefore, the best available approximation of the studied system at $T > −83°C$. Notable are three critical points in the CH$_4$–H$_2$S–CO$_2$ system: C$_1$ and C$_2$ lying along the 2-phase boundary curves, and C$_3$ situated on the 3-phase envelope[58]. The presence of additional gases, e.g., N$_2$ or CH$_4$, is well known to depress the melting points in fluid inclusion gas mixtures[59], however, we assume that N$_2$ quantities as low as 3 mol% would likely have a negligible effect on the phase equilibria. The trajectories followed by studied fluid inclusions (blue) during heating are shown schematically in the P–T space, in the considered diagrams (Fig. 8). The phase transition points (9–15) are indicated by black circles and correspond to numbers given in Table 1.

Cooling of fluid inclusions triggers separation of two phases at temperatures between −33 and −29.5 °C ($\sigma = 1.22$), therefore they follow the trajectory intersecting the dew-point locus and thus enter the L$_2$V 2-phase field (L$_2$—liquid H$_2$S, Fig. 8a). This phase behavior is characteristic for the retrograde system as with decreasing pressure exsolution of the liquid phase takes place instead of the vapor phase. The first appearance of the liquid droplet is difficult to spot meaning that the temperature of condensation may be slightly underestimated. The P–T pathway should intersect the dew curve above the critical point C$_1$, however, the temperature of the V → L$_2$V transition is located below this point in the diagram. This discrepancy stems from the fact that the used phase boundaries were constructed for 40.2 mol % H$_2$S. For lower H$_2$S contents, alike in the studied inclusions
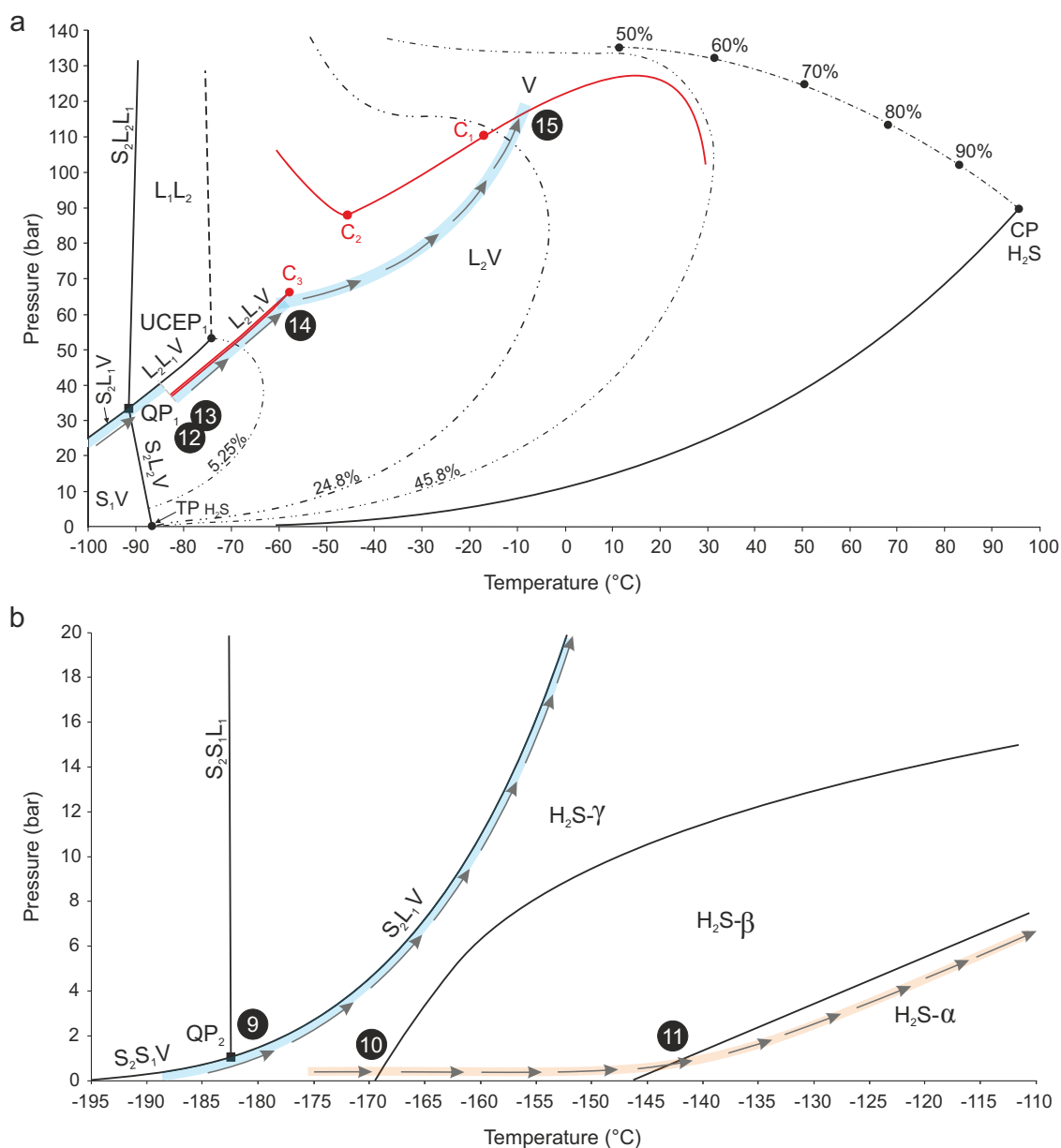
Fig. 8 Phase diagrams schematically illustrating the behavior of studied fluid inclusions in the P–T space. a Simplified phase boundaries for the system $CH_4–H_2S$[31] around critical points and the first invariant point-QP_1 with superimposed phase curves for the $CH_4–H_2S–CO_2$ system[58] (in red). **b** Phase boundaries for the system CH_4-H_2S in the lowest temperature region near the 2nd invariant point-QP_2 point[35] and phase boundaries for pure H_2S at low temperatures[40]. Symbols and abbreviations: upper dash-dotted line-critical curve with marked critical points for various H_2S contents; double-dotted dashed lines-immiscibility loops for 5.25, 24.8, and 45.8 mol% H_2S; thicker pale blue lines and arrows show schematic P–T paths followed by gas inclusions upon heating in the $CH_4–H_2S–CO_2$ and $CH_4–H_2S$ systems, arrows and orange P–T path in the pure H_2S system is followed during solid–solid phase transitions of pure H_2S in the fluid inclusions, numbers in black circles (9–15) correspond to numbers of phase transitions during the heating cycle, which are given in Table 1; C_1, C_2, C_3-critical points in the $CH_4–H_2S–CO_2$ system, CP–H_2S critical point, TP–H_2S triple point, L_2-liquid H_2S, L_1-liquid CH_4, S_2-solid H_2S, S_1-solid CH_4; α, β, γ-solid phases of H_2S.

(25–28 mol%), the dew curve would extend to lower temperatures.

At temperatures between −59.6 and −57.8 °C ($\sigma = 0.63$), closely below the critical point C_3 (−57.5 °C, where $V = L_1$), the fluid inclusion trajectory intersects the 3-phase L_1L_2V boundary emanating from the C_3 point (L_1—liquid CH_4, Fig. 8a). It is manifested by the separation of a third phase in the inclusion and marks the exsolution of a first drop of methane condensate. Under the optical microscope the newly formed phase appears vapor-like (Figs. 2d and 3d), probably due to the very close proximity of the C_3. Since fluid inclusions contain two immiscible

liquid phases and a vapor they follow the path along the L_1L_2V phase boundary and at about −122 °C reach the invariant point: QP_1 (Fig. 8a). At the QP_1, in the $CH_4–H_2S$ system four phases co-exist: solid H_2S-α, liquid H_2S, liquid CH_4 and a vapor[31]. In the analyzed system, the simultaneous and instant solidification of H_2S and CO_2 (Figs. 2e and 3e) is observed, thus in the 3-component $CH_4–H_2S–CO_2$ system five phases co-exist in equilibrium at the invariant quintuple point-QP_1: H_2S solid, CO_2 solid, CH_4 liquid, $H_2S + CO_2$ liquid, and a vapor. If N_2 component is considered the number of phases at equilibrium remains the same, however, the QP_1 is converted into a

univariant curve in the P–T space. The solidification of H_2S–CO_2 is subject to metastability as the measurements of the same inclusion yield a range of temperatures, and similar variability is also reflected by measured FIA1 ($\sigma = 4.58$, Table 1). The freezing temperatures (T_n) are relatively lower compared to melting temperatures (T_m) of H_2S or CO_2 (Table 1), which requires supercooling to nucleate solids. Precipitation of pure solid H_2S-α in the presence of pure solid CO_2 increases the temperature of the QP_1 to between −107 and −104 °C (Table 1), when the cycling technique is applied.

Contemporaneous freezing of H_2S and CO_2 is typically observed in binary H_2S–CO_2 systems at an eutectic temperature of −95.6 °C, where the $S_{CO_2}LV$ and $S_{H_2S}LV$ triple-point loci converge at the quadruple point[32]. The phase behavior, observed in the studied fluid inclusions, can thus be explained by an overlap of quadruple points of the binary CH_4–H_2S and H_2S–CO_2 systems. Moreover, the H_2S-CO_2 freezing point temperatures between −125.9 and −114.9 °C (Table 1), measured in the CH_4–H_2S–CO_2–N_2 inclusion gas phase with 11.9–13.3 mol % CO_2 (in the presence of clathrate, Source Data), are much lower compared to the eutectic temperature for binary H_2S–CO_2 gas mixtures. According to experimental studies, the latter gas mixtures with <12.5 mol% CO_2, follow triple point equilibria with solid H_2S in the binary systems and do not represent eutectic mixtures[32]. Therefore, our study shows that the presence of CH_4 gas has a significant impact on the phase behavior of H_2S–CO_2 gases in studied natural fluid inclusions.

From the QP_1 point onwards fluid inclusions follow the S_2L_1V phase boundary and after intersecting the second quintuple point-QP_2 at temperatures between −188 and −185.3 °C ($\sigma = 0.97$), the S_1S_2V curve becomes a path (Fig. 8b). At the QP_2 two solids: CH_4 (S_1) and H_2S (S_2), liquid CH_4 and vapor phases are co-existing in equilibrium in the CH_4–H_2S system. The position of the QP_2 point in this binary system is determined by SLV equation of state since experimental data are lacking[35]. In the CH_4–H_2S–CO_2 system, five phases co-exist at QP_2: H_2S solid, CO_2 solid, CH_4 solid, CH_4 liquid, and a vapor. Our study shows that both solidification and melting of methane progress gradually over a temperature interval as the liquid/solid methane phase boundary has been clearly observed (Fig. 2h, j). During the latter phase transition five phases: $S_1S_2L_1V$, where S_2 stands for both H_2S and CO_2 solids, are co-existing (Fig. 2h, j). Comparison of T_n and T_m values of CH_4, measured in the inclusion gas mixtures (Table 1), reveals that only slight supercooling is required to nucleate solid CH_4 and it is achievable using liquid N_2 coolant during microthermometry runs.

Melting of methane (point 9 in Fig. 8b) occurs at T_m between −186.3 and −184.1 °C, which are very consistent ($\sigma = 0.3$, Table 1) and lie slightly below the triple point of a pure CH_4 system (−182.48 °C) and a quadruple point-QP_2 of the CH_4–H_2S system (−182.4 °C[35]). The melting temperatures of H_2S-α solid (point 12 in Fig. 8a) within FIA1 (from −98.9 to -98.8 °C) show extremely low variability ($\sigma = 0.05$), which corresponds to stable H_2S contents in the inclusions (Table 1). Solid CO_2 melts (point 13 in Fig. 8a) at temperatures −91.2 °C/−92.6 °C (A/B). Elevated standard deviation ($\sigma = 1.14$) for $T_m(CO_2)$ may be due to slight compositional variation in the inclusions (11.9–13.3 mol% CO_2) or due to difficulties in T_m observations, which stem from a small difference in refractive indices between the liquid phase and very small CO_2 crystals. Melting of all three solids: CH_4, H_2S, and CO_2 proceeds over temperature intervals, which is characteristic of multicomponent gas systems[17,60]. The median T_m values (FIA1): −184.3 °C (CH_4), −98.9 °C (H_2S) and −91.9 °C (CO_2) are depressed compared to temperatures of melting points of the relative unary systems, i.e., −182.5 °C (CH_4), −85.5 °C (H_2S), and −56.6 °C (CO_2). This implies that such melting behavior is not

only typical for multivolatile H_2S-free systems[17], but also for H_2S-rich gas mixtures.

At the point, where the last solid-phase melts, the fluid inclusions follow back the L_1L_2V curve (point 13 in Fig. 8a). The first partial homogenization $T_{h1}(L_1L_2V \rightarrow L_2V)$ takes place in a similar temperature interval from −59.8 to −57.6 °C ($\sigma = 0.78$, point 14 in Fig. 8a) as the relative opposite phase transition during cooling (no. 3 in Table 1). This enforces the inclusions to enter the 2-phase L_2V field (Fig. 8a) until the homogenization to the vapor ($L_2V \rightarrow V$), through a dew-point transition, takes place at temperatures between −32.5 and −28.6 °C ($\sigma = 1.31$). During the latter transition 2-phase fluid inclusions (L_2V) follow back the trajectory intersecting the dew-point locus (point 15 in Fig. 8) and enter the vapor 1-phase field (Fig. 8a).

H_2S solid–solid transitions in fluid inclusions. The observation of low-temperature H_2S solid–solid transitions (α ↔ β ↔ γ) in natural fluid inclusions requires consideration of new phase boundaries: $S_{2\alpha}S_{2\beta}L_1V$ and $S_{2\beta}S_{2\gamma}L_1V$, and their influence on the CH_4–H_2S–CO_2–N_2 system. The experimentally determined solid–solid transitions of pure H_2S occur at temperatures of −169.55 and −146.95 °C[40,42,61], which are above the QP_2 point of the CH_4–H_2S system (Fig. 8b). The temperature range of the H_2S (β → γ) transformations measured in the studied inclusions indicate that the above expected equilibrium temperatures are not sustained along the cooling pathway. In order to nucleate H_2S-γ undercooling or maintaining a constant temperature for a period of time is required, which indicates metastable behavior or kinetics problems. The measured temperatures of the $H_2S(\gamma \rightarrow \beta)$ transition in the studied inclusion are oscillating around an average of −168.1 °C (point 10 in Fig. 8b, Supplementary Table 2), which is slightly higher compared to the corresponding value for a pure H_2S system (−169.55 °C). This may be related to pressure as the P–T diagram for phase transitions of pure (99.5%) solid H_2S, at low pressures, shows that temperatures of solid–solid transitions increase with increasing pressures[40] (Fig. 8b). The H_2S (γ → β) transition is peculiar as after commencement it gradually proceeds even without temperature increase (on hold) with only the laser on, irrespectively of the laser power used. The temperatures of −147 and −146.4 °C for the solid $H_2S(\beta \rightarrow \alpha)$ transitions in the studied fluid inclusion (point 11 in Fig. 8b) are in a very good agreement with the experimentally derived temperature of −146.95 °C (Fig. 8b). According to numerical modeling[35] allotropic behavior of solid H_2S does not affect significantly the overall solid-fluid equilibria of the CH_4–H_2S mixture. Instead, the modeling has shown that in the CH_4–H_2S system the temperatures of solid–solid H_2S transitions are depressed relative to corresponding temperatures in pure H_2S system[35]. This hypothesis is not consistent with $H_2S(\gamma \leftrightarrow \beta \leftrightarrow \alpha)$ transitions temperatures in the natural fluid inclusions studied here and shows that the presence of CH_4–CO_2 gas affects solid–solid H_2S phase equilibria in gas mixtures.

Experimental studies of laboratory-grown H_2S crystals has shown that the solid $H_2S(\gamma \rightarrow \beta)$ transition is attributed to a decrease in the dielectric constant, whereas the $H_2S(\beta \rightarrow \alpha)$ transition is ascribed to orientational ordering relative to the rotational vibrations of the hydrogen atoms[61]. During the higher temperature transition, the crystal structure of both phases (α, β) of fluid inclusion H_2S remains disordered, which is expressed by broad bands observed in the stretching region of the Raman spectrum (Fig. 6) and "blobby" appearance under the optical microscope (Figs. 2g and 3e, f, h, l). The number of peaks and their bandwidths shifts, at the point of the lowest temperature transformation (Fig. 6), imply structural modifications of solid H_2S (Fig. 3i). The crystalline H_2S-γ solid, which nucleates in

natural fluid inclusions, shows peaks at wavenumbers (Fig. 7) very similar to those detected by an experimental study of purified H_2S gas[39]. Microscopic observations during low-temperature runs unambiguously show a structural change to a polycrystalline aggregate with in-situ growing prismatic crystals (Fig. 3i) and confirm the crystalline nature of the studied H_2S-γ phase. Two crystal systems, orthorhombic or tetragonal, were proposed for solid H_2S-γ phase[39,41]. Our study clearly shows that the protracted structural transformations do not immediately follow up the low-temperature phase transitions detected by Raman spectroscopic analyses.

Spectral features of complex gas mixtures. Systematic shifts of Raman peak positions are observed for all inclusion gas species during the measurements. They are most pronounced for H_2S and CH_4 due to their high concentrations in the studied gas-rich inclusions (Figs. 5 and 6). Experimental studies have shown that changes in pressure, temperature and density of a single gas component as well as CH_4–CO_2 gas mixtures have an influence on the Raman peak positions[62–64]. Modifications of gas peak positions in H_2S-bearing ternary, as well as any more complex gas mixtures, have not been studied so far.

Our results show that the Raman band positions are shifted to higher wavenumbers for more volatile components and to lower wavenumbers for less volatile components, relative to the original peak positions of the gas mixture at room temperature (Fig. 5). This tendency is also marked by systematic trends in diagrams illustrating H_2S and CH_4 band positions (cm^{-1}) versus temperature (Fig. 9 and Source Data). It is observed that the FWHM (full width at half maximum) of the peaks of gaseous, liquid, and solid CH_4 phases, which exsolved from the CH_4-H_2S-CO_2-N_2 gas mixture, consistently decrease with decreasing temperatures (Fig. 5). The above-mentioned features reflect well differential partitioning between the co-existing phases in an individual inclusion upon cooling, which is the strongest at the lowest recorded temperatures of about −190 °C (Fig. 9). The observations also reveal that gases of the highest volatility, i.e., N_2 and CH_4, partition into the inner vapor phase, whereas CO_2 and

H_2S partition into the outer liquid phases. Similar distribution of gaseous components between the phases has been described for binary gas mixtures[17]. Our study shows that the composition of the gas mixture affects the wavenumbers of its gas components, e.g., CH_4 peak measured in the gas mixture at room temperature is positioned at 2911 cm^{-1}, whereas at −190 °C it shifts to 2917 cm^{-1} (Fig. 9), which is the wavenumber typical of pure CH_4 gas. The band position downshifts can also be indirectly related to the density difference between gas, liquid, and solid physical states of the inclusion components, i.e., solid H_2S or CH_4 show shifts to the lowest wavenumbers: 2522 and 2904 cm^{-1}, respectively (Fig. 9).

Applications

Experimental models and databases. We report on new fluid inclusion-derived temperature, compositional and spectroscopic data on a multicomponent CH_4–H_2S–CO_2–N_2–H_2O system. The results of our study are helpful not only for the interpretation of phase equilibria observed in fluid inclusion gas mixtures but also can be used as a guide for future experimental studies of fluids utilizing, e.g., synthetic fluid inclusions, fused-silica optical cells, or silica capillary tubes. Such studies are necessary to construct the unified complete topology of the C–O–H–N–S chemical system, which is required to improve understanding of the phase equilibria[29]. Such purely experimental results cannot ideally reproduce natural systems, hence data from natural fluid inclusion gas–H_2O mixtures are complementary and can be used for validation and models refinement. Detailed characterization of phase transition (α ↔ β ↔ γ) temperatures, structural transformations and spectral features of different solid H_2S phases, in natural fluid inclusions, contribute to the advancement of scientific knowledge about the nature of the H_2S solid–solid-phase equilibria.

Our study shows that the band wavenumbers of gas components in the natural CH_4–H_2S–CO_2–N_2 gas mixtures differ from the standard Raman shifts ($\Delta \nu$ in cm^{-1}) known from the Raman databases, and thus have a substantial impact on interpretation of literature data. It has been shown here that gas
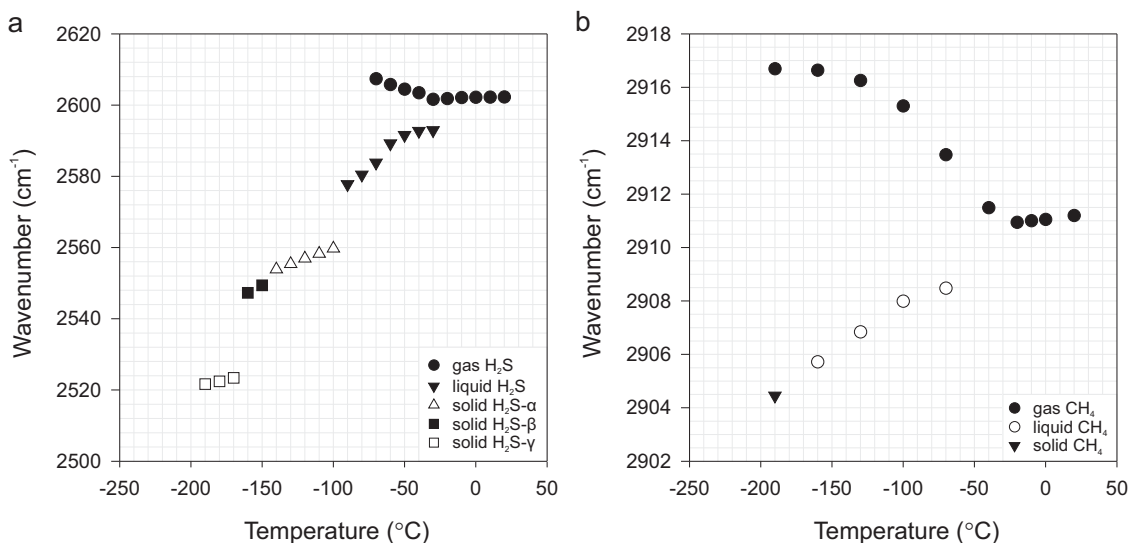

Fig. 9 Diagrams showing the relationship between temperature and Raman band wavenumbers. a Shifts in peak positions of H_2S vapor, liquid, and solid (α, β, γ) phases with decreasing temperature. The measurements were recorded in 10 °C increments. **b** Shifts in band positions of vapor, liquid and solid CH_4 with decreasing temperature. The measurements were recorded in 30 °C increments. Both H_2S and CH_4 show similar trends, namely Raman peak positions of volatile phases shift towards higher wavenumbers, whereas less volatile components reveal opposite tendency. This discrepancy reflects differential partitioning between co-existing phases. The data were collected from one individual fluid inclusion (no. P1a-fi10) during the heating run. The peak positions were calibrated using neon emission lines. See also Source Data file.

peak modifications in ternary H_2S-bearing and more complex gas mixtures depend on their compositions as well as on relative density differences arising from differential partitioning of the gas mixture components in a closed system. These findings constitute new and valuable insights into the behavior of individual gases in multi-gas mixtures in natural fluid systems.

Hydrocarbon and mineral systems. The improved understanding of complex gas–H_2O systems is a prerequisite for more accurate reconstruction of the P–T conditions in hydrocarbon and mineralizing fluid systems in the geological record. The P–T information obtained from studies of fluid inclusions hosted in cements and facture-filling minerals provide means for the reconstruction of multiple fluid and gas migration events in hydrocarbon reservoirs and contribute, e.g., to enhancement of gas accumulation models[22]. The migration of geological fluids, carrying reduced sulfur species (e.g. H_2S, $HS^−$), has a paramount control on the deposition of hydrothermal ore deposits. In evaporitic diagenetic environments of sedimentary basins, hydrocarbon and ore mineral systems are often closely linked[10]. In cases where the circulating basinal brines or formation waters are devoid of sufficient metal content to form sulfide ores, by mixing with H_2S-rich fluids, the latter may accumulate in gas/petroleum traps within sedimentary sequences and may pose risks for hydrocarbon exploration and environmental hazards. Constraining the geological time frames and depth intervals of thermochemical sulfate reduction (TSR)[8] is also of high importance as it produces H_2S and CO_2, which contaminate hydrocarbon reservoirs[6,65,66].

Microthermometric studies of CH_4–H_2S–CO_2–N_2 fluid inclusion gas mixtures allow the prediction of freezing points of H_2S and CO_2. Our study indicates that at low temperatures of about −122 °C (Table 1), the H_2S-CO_2 gases in analyzed gas inclusions show very unique behavior of contemporaneous freezing, which is likely linked to the subordinate amounts of CO_2 (11.9–13.3 mol %). Therefore, CH_4-rich gas mixtures have a potential for relatively efficient purification to commercial quality grades by using, e.g., low-temperature distillation process[38]. However, the disposal of resulting by-products (H_2S, CO_2) rises substantial environmental concerns as geochemical behavior of these gases in various deep geological formations is not yet well constrained[67].

Our study demonstrates that gas-rich CH_4–H_2S–CO_2–N_2–H_2O fluid inclusions offer an excellent opportunity to study the formation of complex natural gas hydrates in a closed system. Due to global warming, there is an increasing interest in understanding the behavior of natural gas hydrates that were discovered in deep-sea environments and permafrost regions[49]. The formation mechanisms, as well as structural and compositional heterogeneities of the complex/mixed natural clathrate crystals, are not yet fully understood[50,51]. Comparison of experimental simulations of synthetic gas hydrates with systematic studies of natural gas–H_2O inclusions mixtures provides means for a better understanding of the kinetics and thermodynamics of clathrates formation and dissociation. Such knowledge is relevant to investigations of synergies between CH_4-gas hydrates and climate change on a global scale[68].

Extraterrestrial systems. Low-temperature systems, which are a prerequisite for solid–solid H_2S transitions do not exist in terrestrial environments, but they persist on ice planets such as Uranus and Neptune[12,13]. Recent studies evidenced the presence of gaseous H_2S above the cloud deck of Uranus, which led to the conclusion that H_2S ice is a major constituent of main clouds at 1.2–3 bar[12]. Similarly, the H_2S ice is considered to be a prime constituent of Neptune's main clouds at pressures of 2.5-3.5 bar[13].

At extremely low temperatures (from ca. −220 °C[11] to −153.7 °C[12]), at various depth levels in the ice giants atmosphere's, there is thus a high likelihood that H_2S ice cloud decks exist in different temperature-dependent solid states. This, in turn, may potentially have an influence on the atmospheric dynamics of the ice planets. Recent studies point also towards differences in the distribution of H_2S ice and CH_4, between polar and equatorial regions of the Uranus's atmosphere, which yet require explanation[12]. The latter could provide valuable insights into the atmospheric dynamics of the enigmatic ice giants[69]. Possible future exploratory missions to the ice planets would benefit from having a Raman spectrometer on board, which allows identification of possible perturbations caused by distinct H_2S solid states and constraining distribution of H_2S ice and associated gases at low temperatures. A miniaturized Raman spectrometer has been used, e.g., in a mission to Mars[70].

Methods

Microthermometry. For this study, we used fracture-filling fluorite mineralization, hosted by Upper Permian Zechstein Ca_2 carbonate from the Southern Permian Basin, Germany. The drill core sample originates from a depth of ca. 3.8 km from well PB-20 situated at the border of the Pompeckj Block and the northern flank of the Lower Saxony Basin[8]. The translucent coarse fluorite crystals, selected for analyses, host abundant CH_4–H_2S–CO_2–N_2–H_2O fluid inclusions (Fig. 1 and Table 1). Doubly-polished fluorite chips (~8 × 8 mm) with a thickness of 180 μm were used for analyses.

Microthermometric and laser Raman spectroscopic measurements were performed at the GFZ Potsdam, Germany. Microthermometry and observations of phase changes in gas-rich inclusions were conducted using a Linkam heating/freezing stage (THMS600 system) that allows observations of phase transitions in fluid inclusions in the temperature range between −195 and 600 °C. The heating/freezing system was calibrated using SynFlinc synthetic fluid inclusion standards: CO_2 and pure H_2O for melting temperatures of CO_2 and ice, respectively as well as critical homogenization temperature of pure H_2O. Temperatures were recorded using Linksys 32 software with reproducibility of ±0.1 °C. Imaging during the microthermometry runs was performed using a digital QICAM FAST1394 camera attached to an Olympus BX53M microscope and the Q-Capture Pro 7 software was used for image acquisition.

Raman spectroscopy combined with microthermometry. Laser Raman spectroscopy coupled with microthermometric experiments was utilized to examine phase changes and solid phases formed at low temperatures. Measurements were performed using the Linkam THMS600 system equipped with LNP95 nitrogen cooling pump, T95 temperature controller, and a stage with a silver heating/freezing block and a PT100 platinum sensor. The Linkam heating-freezing stage was calibrated using the synthetic CO_2 and H_2O fluid inclusion standards, provided by SynFlinc, prior to Raman spectroscopic analyses. The temperatures were recorded, in a range between −192 and +35°C, using a Linksys 32 software with reproducibility of ±0.1 °C. Heating/freezing rates during measurements of the phase transitions were 4 °C/min or/and 10 °C/min, whereas in between the phase transitions the rates were 20–30 °C/min.

The vibrational spectra of phases in gas-rich inclusions during freezing-heating runs were measured using a LabRAM HR Evolution Raman micro-probe supplied by Horiba Scientific. The system is equipped with a dispersive Raman spectrometer with focal length of 800 mm, the frequency-doubled Nd:YAG solid-state green laser source with an excitation radiation of 532 nm and output power of 100 mW (max. ~48 mW at the sample surface), edge filters, and a CCD detector. A grating of 1800 grooves/mm and confocal hole of 100 μm were used, and the spectral resolution was 1 cm^{-1}. Most measurements (when not indicated otherwise) were performed using a neutral density filter, which reduces the output laser power at the sample to 50% (~24 mW) to avoid frequent "out of range" high intensity CH_4 peaks with artificially cut tops. Internal calibration has been performed using a silicon standard (520 cm^{-1}). A neon lamp attached to the Linkam stage was used for a wavenumber calibration. The spectra of Ne emission lines were collected simultaneously with each peak position measurement. The reference Ne emission lines used for the wavenumber calibration of H_2S were: 2389, 2708 cm^{-1}, and of CH_4: 2835, 3006 cm^{-1}. The peak positions, corrected for instrumental drift, were calculated using the measured wavenumbers of H_2S, CH_4 (symmetric stretching v_1 vibrational modes), Ne lines, and applying the linear interpolation equation[71]. The average standard error for peak position measurements at room temperature, based on 8 measurements (2 inclusions measured 4×), was 0.02 cm^{-1} for CH_4 and 0.01 cm^{-1} for H_2S. The uncertainty of the peak wavenumber measurements was ±1 cm^{-1} for all gas components[64].

The Raman spectrometer is adapted to an Olympus BXFM optical microscope, which is equipped with 50× (NA = 0.5) long working distance objective, reflected and transmitted light sources, and a VIS Camera. This setup enables optical

investigation of phase transitions in fluid inclusions as well as photographic documentation during the combined experiments. The Raman spectra were acquired by focusing the laser beam on analyzed phases, in the spectral range between 250 and 4500 cm^{-1} and with 2 × 20s acquisition time. The spectra were processed using LabSpec software (ver. 6.4.4.16). The linear baseline correction and the Gaussian–Lorentzian peak-fitting function were used for processing and deconvolution of the Raman spectra. The concentrations of the aqueous solution (molar fractions) were measured in homogenized inclusion fluid in a temperature range between 160 and 170 °C[45]. Molar fractions of gases in the gas mixtures trapped in inclusions were derived from the ratios of the Raman peak areas and applying the formula based on Placzek's polarizability theory[23,29,62]. The average standard error for estimation of mole fractions, based on 14 measurements (2 inclusions measured 7×), was 0.001 cm^{-1} for each gas component.

Data availability

All relevant data that support the findings of this study are available within the paper. The Raman spectroscopy and microthermometry data generated in this study are provided in the Supplementary Information and Source Data files. Source data are provided with this paper.

References

1. Machel, H. G. Bacterial and thermochemical sulfate reduction in diagenetic settings - old and new insights. *Sediment. Geol.* **140**, 143–175 (2001).
2. Olson, K. R. & Straub, K. D. The role of hydrogen sulfide in evolution and the evolution of hydrogen sulfide in metabolism and signaling. *Physiology* **31**, 60–72 (2016).
3. Mißbach, H. et al. Ingredients for microbial life preserved in 3.5 billion-year-old fluid inclusions. *Nat. Commun.* **12**, 1101 (2021).
4. Berresheim, H. & Jaeschke, W. The contribution of volcanoes to the global atmospheric sulfur budget. *J. Geophys. Res. Oceans* **88**, 3732–3740 (1983).
5. Von Damm, K. L. Seafloor hydrothermal activity: black smoker chemistry and chimneys. *Annu. Rev. Earth Planet. Sci.* **18**, 173–204 (1990).
6. Worden, R. H. & Smalley, P. C. H_2S-producing reactions in deep carbonate gas reservoirs: Khuff Formation, Abu Dhabi. *Chem. Geol.* **133**, 157–171 (1996).
7. Yang, C., Hutcheon, I. & Krouse, H. R. Fluid inclusion and stable isotopic studies of thermochemical sulphate reduction from Burnt Timber and Crossfield East gas fields in Alberta, Canada. *Bull. Can. Pet. Geol.* **49**, 149–164 (2001).
8. Sośnicka, M. & Lüders, V. Fluid inclusion evidence for low-temperature thermochemical sulfate reduction (TSR) of dry coal gas in Upper Permian carbonate reservoirs (Zechstein, Ca2) in the North German Basin. *Chem. Geol.* **534**, 119453 (2020).
9. Mernagh, T. P. & Bastrakov, E. N. An evaluation of hydrogen sulfide in orogenic gold fluids and the uncertainties associated with vapor-rich inclusions. *Geofluids* **13**, 494–505 (2013).
10. Sośnicka, M. & Lüders, V. Super-deep, TSR-controlled Phanerozoic MVT type Zn-Pb deposits hosted by Zechstein-2 gas reservoir carbonate (Ca2), Lower Saxony Basin, Germany. *Chem. Geol.* **508**, 62–77 (2019).
11. Helled, R., Nettelmann, N. & Guillot, T. Uranus and Neptune: origin, evolution and internal structure. *Space Sci. Rev.* **216**, 38 (2020).
12. Irwin, P. G. J. et al. Detection of hydrogen sulfide above the clouds in Uranus's atmosphere. *Nat. Astron* **2**, 420–427 (2018).
13. Irwin, P. G. J. et al. Probable detection of hydrogen sulphide (H_2S) in Neptune's atmosphere. *Icarus* **321**, 550–563 (2019).
14. Drozdov, A. P., Eremets, M. I., Troyan, I. A., Ksenofontov, V. & Shylin, S. I. Conventional superconductivity at 203 kelvin at high pressures in the sulfur hydride system. *Nature* **525**, 73–76 (2015).
15. Snider, E. et al. Room-temperature superconductivity in a carbonaceous sulfur hydride. *Nature* **586**, 373–377 (2020).
16. Roedder, E. *Fluid Inclusions. Reviews in Mineralogy* Vol. 12 (Mineralogical Society of Amer, 1984).
17. Diamond, L. W. in *Fluid Inclusions: Analysis and Interpretation. Mineralogical Association Canada, Short Course 32* (eds. Samson, I., Anderson, A. & Marshall, D.) Vol. 32, 101–158 (2003).
18. Diamond, L. W. in *Fluid Inclusions: Analysis and Interpretation. Mineralogical Association Canada, Short Course 32* (eds. Samson, I., Anderson, A. & Marshall, D.) Vol. 32 55–79 (2003).
19. Thiery, R., van den Kerkhof, A. M. & Dubessy, J. vX-properties of CH_4-CO_2 and CO_2-N_2 fluid inclusions modelling for T<31°C and P<400 bars. *Eur. J. Mineral.* **6**, 753–771 (1994).
20. Burruss, R. C., Cercone, K. R. & Harris, P. M. in *Carbonate Cements* (eds. Schneidermann, N. & Harris, P. M.) 277–289 (Society of Economic Paleontologists and Mineralogists, 1985).
21. Lüders, V. et al. Fluid and gas migration in the North German Basin: fluid inclusion and stable isotope constraints. *Int. J. Earth Sci. (Geol. Rundsch.)* **94**, 990–1009 (2005).
22. Fall, A. et al. Testing the basin-centered gas accumulation model using fluid inclusion observations: Southern Piceance Basin, Colorado. *AAPG Bull.* **96**, 2297–2318 (2012).
23. Burke, E. A. J. Raman microspectrometry of fluid inclusions. *Lithos* **55**, 139–158 (2001).
24. Klemd, R., Hirdes, W., Olesch, M. & Oberthür, T. Fluid inclusions in quartz-pebbles of the gold-bearing Tarkwaian conglomerates of Ghana as guides to their provenance area. *Mineral. Depos.* **28**, 334–343 (1993).
25. Zwahlen, C. et al. Constraining the fluid history of a CO_2-H_2S reservoir: insights from stable isotopes, REE, and fluid inclusion microthermometry. *Geochem. Geophys. Geosyst.* **20**, 359–382 (2019).
26. Roedder, E. & Bodnar, R. J. Geologic pressure determinations from fluid inclusion studies. *Annu. Rev. Earth Planet. Sci.* **8**, 263–301 (1980).
27. Duan, Z., Møller, N. & Weare, J. H. A general equation of state for supercritical fluid mixtures and molecular dynamics simulation of mixture PVTX properties. *Geochim. Cosmochim. Acta* **60**, 1209–1216 (1996).
28. Bakker, R. J. Package FLUIDS. Part 3: correlations between equations of state, thermodynamics and fluid inclusions. *Geofluids* **9**, 63–74 (2009).
29. Dubessy, J., Poty, B. & Ramboz, C. Advances in C-O-H-N-S fluid geochemistry based on micro-Raman spectrometric analysis of fluid inclusions. *Eur. J. Miner.* **1**, 517–534 (1989).
30. Touray, J.-C. & Guilhaumou, N. Characterization of H_2S bearing fluid inclusions. *Bull. Minéral.* **107**, 181–188 (1984).
31. Kohn, J. P. & Kurata, F. Heterogeneous phase equilibria of the methane—hydrogen sulfide system. *AIChE J.* **4**, 211–217 (1958).
32. Sobocinski, D. P. & Kurata, F. Heterogeneous phase equilibria of the hydrogen sulfide–carbon dioxide system. *AIChE J.* **5**, 545–551 (1959).
33. Sakoda, N. & Uematsu, M. A thermodynamic property model for the binary mixture of methane and hydrogen sulfide. *Int. J. Thermophys.* **26**, 1303–1325 (2005).
34. Coquelet, C. et al. Phase equilibrium data for the hydrogen sulphide+methane system at temperatures from 186 to 313K and pressures up to about 14MPa. *Fluid Phase Equilibria* **383**, 94–99 (2014).
35. Langè, S., Campestrini, M. & Stringari, P. Phase behavior of system methane + hydrogen sulfide. *AIChE J.* **62**, 4090–4108 (2016).
36. Hensel, W. E. & Massoth, F. E. Phase equilibria for the ternary system: CH_4-CO_2-H_2S. *J. Chem. Eng. Data* **9**, 352–356 (1964).
37. Morris, J. S. & Byers, C. H. Near-critical-region equilibria of the CH_4-CO_2-H_2S system. *Fluid Phase Equilib.* **66**, 291–308 (1991).
38. Langé, S., Pellegrini, L. A., Stringari, P. & Coquelet, C. Experimental determination of the solid-liquid-vapor locus for the CH_4-CO_2-H_2S system and application to the design of a new low-temperature distillation process for the purification of natural gas. *AIChE J.* **hal-01250866**, 1–32 (2015).
39. Miller, R. E. & Leroi, G. E. Raman spectra of polycrystalline H_2S and D_2S. *J. Chem. Phys.* **49**, 2789–2797 (1968).
40. Stewart, J. W. Compression and phase transitions of solid NH_3, SiF_4, H_2S, and CF_4. *J. Chem. Phys.* **33**, 128–133 (1960).
41. Sándor, E. & Ogunade, S. O. Structure and phase transition in solid hydrogen and deuterium sulphides. *Nature* **224**, 905–907 (1969).
42. Shimizu, H. et al. Pressure-temperature phase diagram of solid hydrogen sulfide determined by Raman spectroscopy. *Phys. Rev. B* **51**, 9391–9394 (1995).
43. Murphy, G. M. & Vance, J. E. Raman spectra of hydrogen and deuterium sulfides in the gas, liquid and solid states. *J. Chem. Phys.* **6**, 426–429 (1938).
44. Goldstein, R. H. & Reynolds, T. J. *Systematics of Fluid Inclusions in Diagenetic Minerals Short Course*. Vol. 31 (Society for Sedimentary Geology SEPM, 1994).
45. Berkesi, M. et al. Detection of small amounts of H_2O in CO_2-rich fluid inclusions using Raman spectroscopy. *J. Raman Spectrosc.* **40**, 1461–1463 (2009).
46. Bakker, R. J. & Diamond, L. W. Estimation of volume fractions of liquid and vapor phases in fluid inclusions, and definition of inclusion shapes. *Am. Mineral.* **91**, 635–657 (2006).
47. Dubessy, J., Lhomme, T., Boiron, M.-C. & Rull, F. Determination of chlorinity in aqueous fluids using raman spectroscopy of the stretching band of water at room temperature: application to fluid inclusions. *Appl. Spectrosc.* **56**, 99–106 (2002).
48. Liu, C., Lu, H. & Ye, Y. Raman spectroscopy of nitrogen clathrate hydrates. *Chin. J. Chem. Phys.* **22**, 353–358 (2009).
49. Chazallon, B., Focsa, C., Charlou, J.-L., Bourry, C. & Donval, J.-P. A comparative Raman spectroscopic study of natural gas hydrates collected at different geological sites. *Chem. Geol.* **244**, 175–185 (2007).
50. Schicks, J. M. et al. A new high-pressure cell for systematic in situ investigations of micro-scale processes in gas hydrates using confocal micro-Raman spectroscopy. *Rev. Sci. Instrum.* **91**, 115103 (2020).
51. Sloan, E. D. & Koh, C. *Clathrate Hydrates of Natural Gases* (CRC Press, 2008).
52. Dubessy, J., Boiron, M.-C., Moissette, A., Monnin, C. & Sretenskaya, N. Determinations of water, hydrates and pH in fluid inclusions by micro-Raman spectrometry. *Eur. J. Miner.* **4**, 885–894 (1992).

53. Bény, C., Guilhaumou, N. & Touray, J.-C. Native sulphur-bearing fluid inclusions in the CO_2-H_2S-H_2O-S system—microthermometry and Raman microprobe (MOLE) analysis - thermochemical interpretations. *Chem. Geol.* **37**, 113–127 (1982).

54. Zwart, E. W. & Touret, J. L. R. Melting behaviour and composition of aqueous fluid inclusions in fluorite and calcite: applications within the system H_2O-$CaCl_2$-NaCl. *Eur. J. Mineral.* 773–786 (1994).

55. Sum, A. K., Burruss, R. C. & Sloan, E. D. Measurement of clathrate hydrates via Raman spectroscopy. *J. Phys. Chem. B* **101**, 7371–7377 (1997).

56. Suleimenov, O. M. & Krupp, R. E. Solubility of hydrogen sulfide in pure water and in NaCl solutions, from 20 to 320°C and at saturation pressures. *Geochim. Cosmochim. Acta* **58**, 2433–2444 (1994).

57. Guilhaumou, N., Velde, B. & Beny, C. Raman microprobe analysis of gaseous inclusion in diagenetically recrystallized calcites. *Bull. Minéral.* **107**, 193–202 (1984).

58. Ng, H.-J., B. Robinson, D. & Leu, A.-D. Critical phenomena in a mixture of methane, carbon dioxide and hydrogen sulfide. *Fluid Phase Equilib.* **19**, 273–286 (1985).

59. Burruss, R. C. Analysis of fluid inclusions; phase equilibria at constant volume. *Am. J. Sci.* **281**, 1104–1126 (1981).

60. Van den Kerkhof, A. M. Isochoric phase diagrams in the systems CO_2-CH_4 and CO_2-N_2: application to fluid inclusions. *Geochim. Cosmochim. Ac* **54**, 621–629 (1990).

61. Giauque, W. F. & Blue, R. W. Hydrogen sulfide. The heat capacity and vapor pressure of solid and liquid. the heat of vaporization. A comparison of thermodynamic and spectroscopic values of the entropy. *J. Am. Chem. Soc.* **58**, 831–837 (1936).

62. Seitz, J. C., Pasteris, J. D. & Chou, I.-M. Raman spectroscopic characterization of gas mixtures. II. Quantitative composition and pressure determination of the CO_2-CH_4 system. *Am. J. Sci.* **296**, 577–600 (1996).

63. Jiang, L., Xin, Y., Chou, I.-M. & Chen, Y. Raman spectroscopic measurements of v_1 band of hydrogen sulfide over a wide range of temperature and density in fused-silica optical cells. *J. Raman Spectrosc.* **49**, 343–350 (2017).

64. Bakker, R. J. The perfection of Raman spectroscopic gas densimeters. *J. Raman Spectrosc.* 1–26, https://doi.org/10.1002/jrs.6245 (2021).

65. Machel, H. Geological and hydrogeological evaluation of the Nisku Q-Pool in Alberta, Canada, for H_2S and/or CO_2 storage. *Oil Gas. Sci. Technol.* **60**, 51–65 (2005).

66. Cai, C. et al. Methane-dominated thermochemical sulphate reduction in the Triassic Feixianguan formation East Sichuan Basin, China: towards prediction of fatal H_2S concentrations. *Mar. Pet. Geol.* **21**, 1265–1279 (2004).

67. Pironon, J., Jacquemet, N., Lhomme, T. & Teinturier, S. Fluid inclusions as micro-samplers in batch experiments: a study of the system C-O-H-S-cement for the potential geological storage of industrial acid gas. *Chem. Geol.* **237**, 264–273 (2007).

68. Ruppel, C. D. & Kessler, J. D. The interaction of climate change and methane hydrates. *Rev. Geophys.* **55**, 126–168 (2017).

69. Tollefson, J., Pater, I., de, Luszcz-Cook, S. & DeBoer, D. Neptune's latitudinal variations as viewed with ALMA. *Astron. J* **157**, 251 (2019).

70. Brolly, C., Parnell, J. & Bowden, S. Raman spectroscopy: caution when interpreting organic carbon from oxidising environments. *Planet. Space Sci.* **121**, 53–59 (2016).

71. Lin, F., Bodnar, R. J. & Becker, S. P. Experimental determination of the Raman CH_4 symmetric stretching (v1) band position from 1–650bar and 0.3–22 °C: application to fluid inclusion studies. *Geochim. Cosmochim. Acta* **71**, 3746–3756 (2007).

Author contributions
V.L. studied phase transitions in numerous C–O–H–N–S fluid inclusions microscopically for a pre-selection of fluid inclusions used in this study. M.S. carried out micro-thermometry and Raman spectroscopy of selected fluid inclusions, interpreted the results, and wrote the manuscript. V.L. contributed to writing and the discussion of the results. Both authors contributed to the concept and design of the experiments.

Competing interests
The authors declare no competing interests.

Additional information
Supplementary information The online version contains supplementary material available at https://doi.org/10.1038/s41467-021-27269-6.

Correspondence and requests for materials should be addressed to Marta Sośnicka.

Peer review information *Nature Communications* thanks Ronald Bakker, David Sublett and the anonymous reviewer(s) for their contribution to the peer review of this work.

Reprints and permission information is available at http://www.nature.com/reprints

Publisher's note Springer Nature remains neutral with regard to jurisdictional claims in published maps and institutional affiliations.